11 Detector performance

11.1 Requirements

The main purpose of the TRD is to provide electron identification and tracking in the momentum range above 1 GeV/c . Therefore it has to be assured that a sufficient pion suppression can be achieved, even in the high multiplicity environment expected in the ALICE experiment. Additionally, a high tracking efficiency and good momentum resolution for particles in the momentum range of interest is required. In Chapter 1 the physics objectives and the correspondingly following detector requirements are already described. Table 11.1 summarizes again the basic requirements on the detector performance that have to be achieved.

Table 11.1: Detector requirements.

momentum resolution	5% (for $p = 5\,\mathrm{GeV}/c$)
tracking efficiency	90% (for $p > 1\,\mathrm{GeV}/c$)
π-rejection factor	100 (for 90% e-efficiency and $p_\mathrm{t} \geq 3\,\mathrm{GeV}/c$)

11.2 Simulation of the detector response

In order to study the performance of the TRD detector in a high multiplicity environment, a detailed simulation of the detector response is necessary. The output of this simulation should be as close as possible to the raw data that will be produced in a real experimental run. This allows to apply the same reconstruction software to simulated data that later on will be used for the analysis of the real data.

In the following the procedure to simulate the detector response is described. It can be divided into two basic steps: The first is the generation of electron clusters in the drift volume by the energy loss of charged particles and the absorption of TR-photons. The second step involves the transformation of the deposited charge into raw-data like ADC-signals, which then can serve as input to the reconstruction. Boths steps are implemented in AliRoot [1], the ALICE software package, which provides an object oriented framework for the simulation and the reconstruction. Therefore most of the software is written in C++ and based on the ROOT package [2], although for the tracking of Monte Carlo generated particles routines from GEANT 3.21 [3] are used.

Throughout this chapter the cartesian coordinates (x, y, z) are in the coordinate frame of a single readout chamber. The z-direction is parallel to the beam axis, y is the direction parallel to the anode wires and follows the $r\varphi$-direction of the detector, and x is the drift direction. The Color Fig. 3 shows the geometry of the TRD as it is implemented in the AliRoot package.

11.2.1 Energy loss

The simulation of the energy loss in the TRD gas follows in principle the same recipe already employed for the ALICE TPC [5]. In a first step the electromagnetic interaction of a charged particle releases primary electrons from the atoms of the TRD gas. The probability for primary ionization as a function of the distance s travelled follows an exponential probability distribution [6, 7]:

$$P(s) = \frac{1}{D} \exp\left(\frac{-s}{D}\right). \tag{11.1}$$

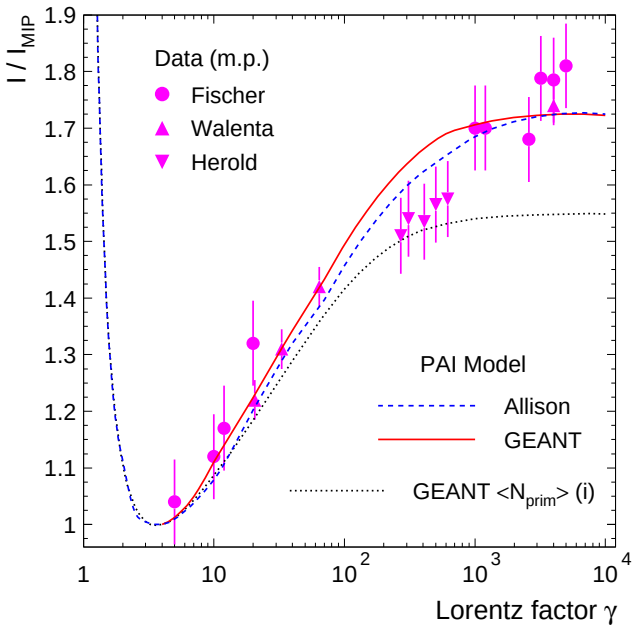

Figure 11.1: The relativistic rise for Xe gas, given most probable (m.p.) values, normalized to MIP case ($\gamma = 4$). The symbols represent the available measurements and the lines show model predictions.

Here D denotes the mean distance between the primary ionizations and is defined as:

$$D = \frac{1}{\langle N_{\text{prim}} \rangle \, f(\beta\gamma)}. \tag{11.2}$$

The quantity $\langle N_{\text{prim}} \rangle$ is the average number of primary electrons per cm created by a minimum ionizing particle (MIP) and $f(\beta\gamma) = I/I_{\text{MIP}}$ is the Bethe-Bloch curve. There are large differences in the literature concerning the value of $\langle N_{\text{prim}} \rangle$ and the height of the Fermi plateau of the Bethe-Bloch curve for Xe, as is illustrated by Table 11.2:

Table 11.2: Different parameters concerning the primary ionization of MIPs.

	GEANT [3]	Sauli [8]	Ermilova [4]
$\langle N_{\text{prim}} \rangle$ (1/cm)	20.5	44.0	48.0
Fermi plateau (mean)	1.56	-	1.36

In Fig. 11.1 we show the magnitude of the relativistic rise for Xe in terms of the most probable (m.p.) values. All values are normalized to the MIP case ($\gamma = 4$). The average values of the number of primary collisions per cm, $\langle N_{\text{prim}} \rangle(i)$, as calculated using GEANT is the input to the simulations. The resulting most probable values of the energy deposit are plotted as solid line. The results of the simulation are compared to the existing measured data [9–11], to which they agree well. Also included is a Photon Absorption and Ionization (PAI) model calculation (dashed line, labelled Allison) [12], giving very similar results (naturally, as GEANT is using PAI for the calculation of $\langle N_{\text{prim}} \rangle$). A similar agreement to the experimental data was obtained by a PAI implementation in GEANT4 [13].

If a charged particle is found to be passing through the Xe filled drift volume of a readout chamber, its average step size is set according to eq.11.2. After each step, calculated using Eq. 11.1, a primary

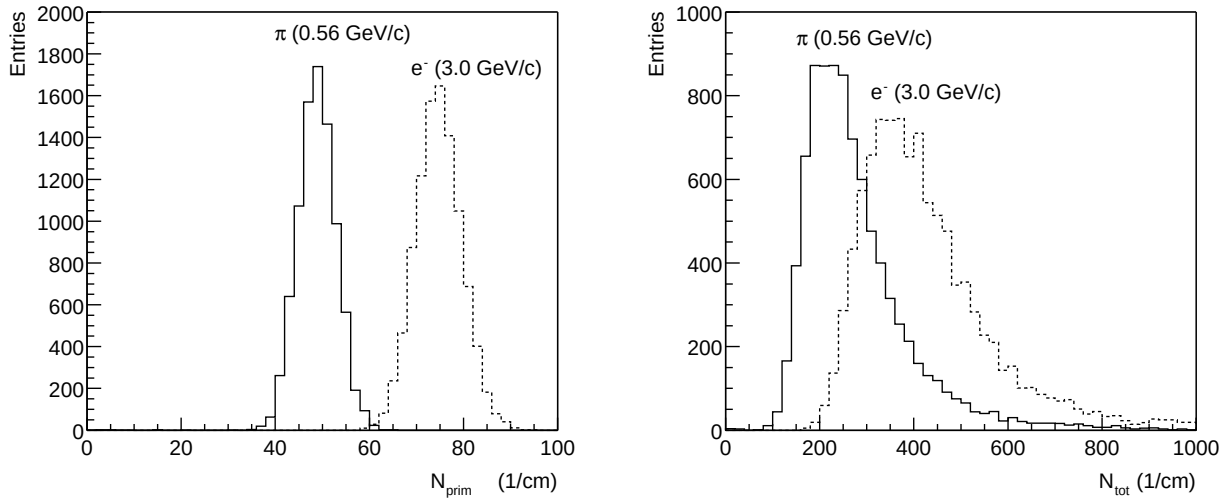

Figure 11.2: The distribution of the number of primary electrons N_{prim} (left panel) and of the total number of electrons N_{tot} (right panel).

ionization process is assumed and correspondingly an electron cluster is created. The left panel of Fig. 11.2 contains the distribution of the number of primary electrons (i.e. number of electron clusters) N_{prim} for a MIP (0.56 GeV/c pions, solid line) and for 3.0 GeV/c electrons (dashed line). According to the Ermilova value of $\langle N_{\text{prim}} \rangle$ chosen in this simulation, the MIP distribution centers around 48.0/cm.

In order to determine the number of electrons in each cluster, the energy spectrum of the primary electrons has to be known. Due to the lack of measurements for Xe, one has to rely on models here. Based on the PAI model, the authors of [4] derive a spectrum, which results in reasonable values for the average ionization energy loss and which is therefore implemented in our simulation. Figure 11.3 displays this distribution (labelled Ermilova) and also includes a comparison to a distribution taken from GEANT [3] (using the X-ray cross sections from Sandia) and a $1/E$ distribution, which is frequently used for these purposes [8]. The curves in Fig. 11.3 are the integrated distributions

$$\left(\frac{\mathrm{d}N}{\mathrm{d}x}\right)_{>E} = \int_E^\infty \frac{\mathrm{d}^2N}{\mathrm{d}x\mathrm{d}E'}\,\mathrm{d}E' \tag{11.3}$$

and therefore represent the number of inelastic collisions per cm with an energy transfer above E. The distributions start at the first ionization potential, which is I_{pot} =12.1 eV for Xe, and extends into the region where GEANT starts generating tracks from δ-rays ($>10\,$keV). We have chosen the Ermilova model and the GEANT Fermi plateau in our simulations, since this generates a higher ionization and therefore represents a worst case estimate in view of the particle identification capabilities. Note also that the simulation of the energy loss is done for pure Xe gas. For the actually used gas mixture (Xe,CO_2 (15%)) the ionization is additionally lower than what is implemented in the simulation.

Following the above described procedure, after each inelastic collision an electron cluster is produced. The number of electrons contained in this cluster N_{tot} is determined by the energy of the primary electron E, which is chosen according to the Ermilova distribution, and the effective energy W that is required to produce a free electron ($W \simeq 22$ eV for Xe).

$$N_{\text{tot}} = \frac{E - I_{\text{pot}}}{W} + 1 \tag{11.4}$$

The right panel of Fig. 11.2 shows the distribution of the total number of electrons N_{tot} per cm in Xe for a MIP (0.56 GeV/c pions, solid line) and for 3.0 GeV/c electrons (dashed line). The mean value for a MIP is 280 e^-/cm and 425 e^-/cm for 3.0 GeV/c electrons.

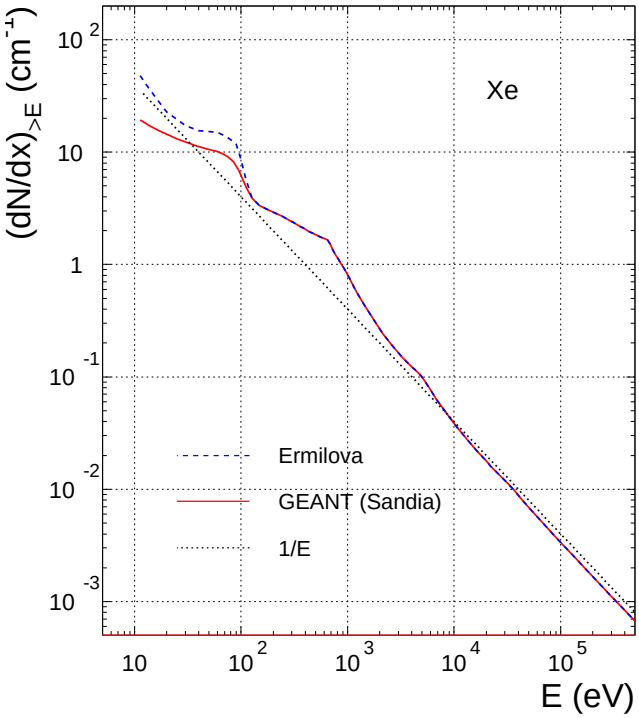

Figure 11.3: The number of inelastic collisions per unit length releasing a primary electron with energy E as a function of the energy for Xe gas.

The Color Fig. 4 shows an event display with the simulated hits in the TPC and TRD generated in the above described way for particles of different species. One can clearly recognize the tracklets in the 6 TRD layers.

11.2.2 Transition radiation

For the study of the electron identification capabilities the production of transition radiation (TR) has to be part of the simulation. Since this is not included in GEANT 3.21 it had to be added to AliRoot. A straightforward calculation of a TR spectrum is only possible for a regular structure of interfaces like it is realized in a foilstack radiator. The following section therefore describes how this is done in this case and what is used within the simulation code.

Theory of TR

A practical theory of the TR production is presented in ref. [14–16]. Here only the most important results are summarized.

The energy density spectrum radiated at polar angle θ by a charged particle with the Lorentz factor γ traversing an interface between two dielectric media (with the dielectric constants ε_1 and ε_2) has the following expression:

$$\frac{d^2W}{d\omega d\Omega} = \frac{\alpha}{\pi^2}\left(\frac{\theta}{\gamma^{-2}+\theta^2+\xi_1^2} - \frac{\theta}{\gamma^{-2}+\theta^2+\xi_2^2}\right)^2. \tag{11.5}$$

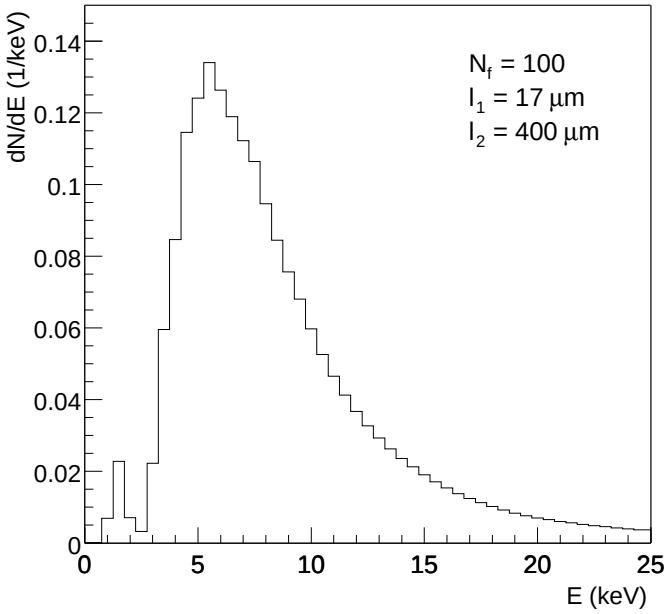

Figure 11.4: The energy spectrum of the TR photons calculated using eq.11.14 together with the parameters given in Table 11.3.

This is deduced for $\gamma \gg 1, \quad \xi_1^2, \xi_2^2 \ll 1, \quad \theta \ll 1$. Here $\xi_i^2 = \omega_{P,i}^2/\omega^2 = 1 - \varepsilon_i(\omega)$, where $\omega_{P,i}$ is the plasma frequency for the two media and α is the fine structure constant (α = 1/137). The plasma frequency is a material property and has the following expression:

$$\omega_P = \sqrt{\frac{4\pi\alpha n_e}{m_e}} = 28.8\sqrt{\rho\frac{Z}{A}} \quad \text{eV}\,, \tag{11.6}$$

where n_e and m_e are the electron density in the material and the electron mass. Typical values for plasma frequency are ω_{P,CH_2} = 20 eV, $\omega_{P,Air}$ = 0.7 eV.

As the emission angle of the TR is small ($\theta \simeq 1/\gamma$) one usually integrates over the solid angle and gets the (differential) energy spectrum:

$$\left(\frac{dW}{d\omega}\right)_{\text{interface}} = \frac{\alpha}{\pi}\left[\frac{\xi_1^2+\xi_2^2+2\gamma^{-2}}{\xi_1^2-\xi_2^2}\ln\left(\frac{\gamma^{-2}+\xi_1^2}{\gamma^{-2}+\xi_2^2}\right)-2\right]. \tag{11.7}$$

For one foil one has to sum up the contributions of the two interfaces, resulting in the expression:

$$\left(\frac{d^2W}{d\omega d\Omega}\right)_{\text{foil}} = \left(\frac{d^2W}{d\omega d\Omega}\right)_{\text{interface}} \times 4\sin^2(\varphi_1/2), \tag{11.8}$$

where $4\sin^2(\varphi_1/2)$ is the interference factor.

For a stack of N_f foils of thickness l_1, separated by a medium (usually a gas) of thickness l_2, one has:

$$\left(\frac{d^2W}{d\omega d\Omega}\right)_{\text{stack}} = \left(\frac{d^2W}{d\omega d\Omega}\right)_{\text{foil}} \times \exp\left(\frac{1-N_f}{2}\sigma\right)\frac{\sin^2(N_f\varphi_{12}/2)+\sinh^2(N_f\sigma/4)}{\sin^2(\varphi_{12}/2)+\sinh^2(\sigma/4)}, \tag{11.9}$$

where $\varphi_{12} = \varphi_1 + \varphi_2$ is the phase retardation, $\varphi_i \simeq (\gamma^{-2}+\theta^2+\xi_i^2)\omega l_i/2$ and $\sigma = \sigma_1 + \sigma_2$ is the total absorption cross section for the radiator (foil + gas).

The TR produced by a multifoil radiator can be characterized by the following qualitative features:

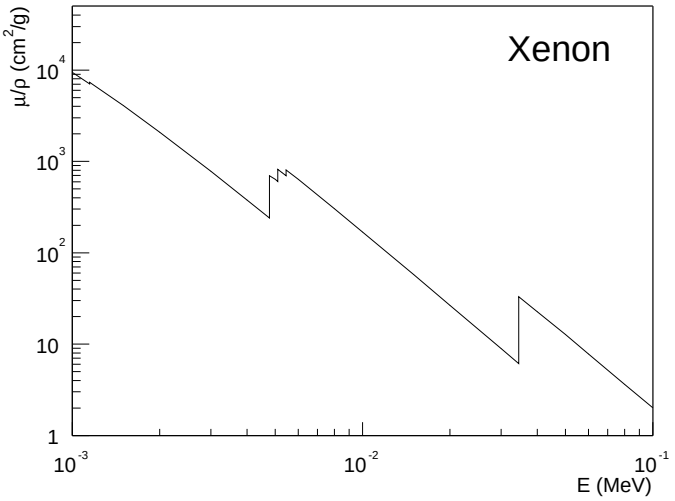

Figure 11.5: The mass attenuation coefficient μ/ρ in Xe gas [19].

- One can define the so-called "formation zone": $Z_i = (\gamma^{-2} + \theta^2 + \xi_i^2)^{-1} 2/\omega$, which is interpreted as the distance after which the separation between particle and emitted photon is of the order of the photon wavelength [14]. The yield is suppressed if $l_i \ll Z_i$ and this is called "formation zone effect".
  In the opposite case $l_i \gg Z_i$ interference can be neglegted and one has:

$$\left(\frac{d^2W}{d\omega d\Omega}\right)_{foil} = 2 \times \left(\frac{d^2W}{d\omega d\Omega}\right)_{interface}; \quad \left(\frac{d^2W}{d\omega d\Omega}\right)_{stack} = N_f \times \left(\frac{d^2W}{d\omega d\Omega}\right)_{foil}. \tag{11.10}$$

- The TR spectrum has the most relevant maximum at $\omega_{max} = l_1 \omega_{P,1}^2/2\pi$ and this allows the "tuning" of the performance of a TRD by varying the material and thickness of the radiator foils.
- For $l_2/l_1 \gg 1$ the TR spectrum is mainly determined by the single foil interference.
- The multiple foil interference governs the saturation at high γ, above the value:

$$\gamma_s = \frac{1}{4\pi}\left[(l_1 + l_2)\omega_{P,1} + \frac{1}{\omega_{P,1}}(l_1\omega_{P,1}^2 + l_2\omega_{P,2}^2)\right]. \tag{11.11}$$

A convenient way to study the TR features is to use scaled variables [15]:

$$\Gamma = \gamma/\gamma_1, \quad \nu = \omega/\omega_1, \tag{11.12}$$

where $\gamma_1 = l_1\omega_{P,1}/2, \quad \omega_1 = \gamma_1\omega_{P,1}$. In terms of the above variables, the TR production of a foil can then be written as:

$$\left(\frac{dW}{d\omega}\right)_{foil} = \frac{2\alpha}{\pi} G(\nu, \Gamma). \tag{11.13}$$

A simple expression that describes the TR production and is used in our simulation is the following [17]:

$$\frac{dW}{d\omega} = \frac{4\alpha}{\sigma(\kappa+1)}(1 - \exp(-N_f\sigma)) \times \sum_{n=1}^{\infty} \theta_n \left(\frac{1}{\rho_1 + \theta_n} - \frac{1}{\rho_2 + \theta_n}\right)^2 [1 - \cos(\rho_1 + \theta_n)], \tag{11.14}$$

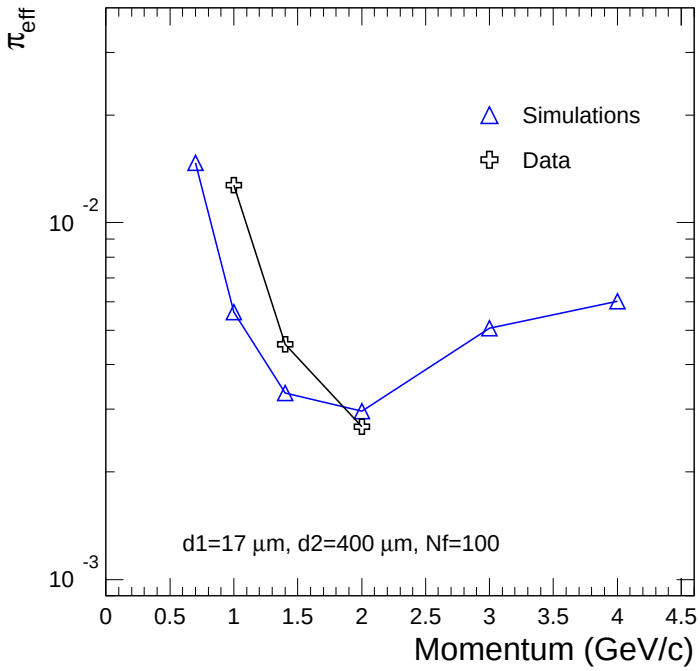

Figure 11.6: The simulated momentum dependence of the pion efficiency for isolated tracks together with results from the test beam measurements.

where:

$$\rho_i = \omega l_1/2c(\gamma^{-2}+\xi_1^2), \quad \kappa = l_2/l_1, \quad \theta_n = \frac{2\pi n-(\rho_1+\kappa\rho_2)}{1+\kappa} > 0. \tag{11.15}$$

Implementation in simulation

For each electron entering the drift volume of a readout chamber, TR photons are created with a distribution described by Eq. 11.14 (see Fig. 11.4). The position of the absorption of the TR photons is determined by the mass attenuation coefficient μ/ρ (shown for pure Xe gas in Fig. 11.5, in the simulation μ/ρ for the Xe,CO_2 (15%) gas mixture is used) and the direction of the incoming particle, defined by its momentum components. If the absorption is inside the gas volume a hit is created at this point whose charge content is given by

$$N_{tot}^{TR} = \frac{E_{TR}-I_{pot}}{W}+1, \tag{11.16}$$

where E_{TR} is the energy of a given TR photon.

Table 11.3: Parameters in the TR photon simulation.

Number of foils N_f	100
Thickness of the foils l_1	17 μm
Thickness of the gaps l_2	400 μm
Density of the foils ρ_1	0.92 g/cm^3
Density of the gas ρ_2	$1.977 \cdot 10^{-3}$ g/cm^3

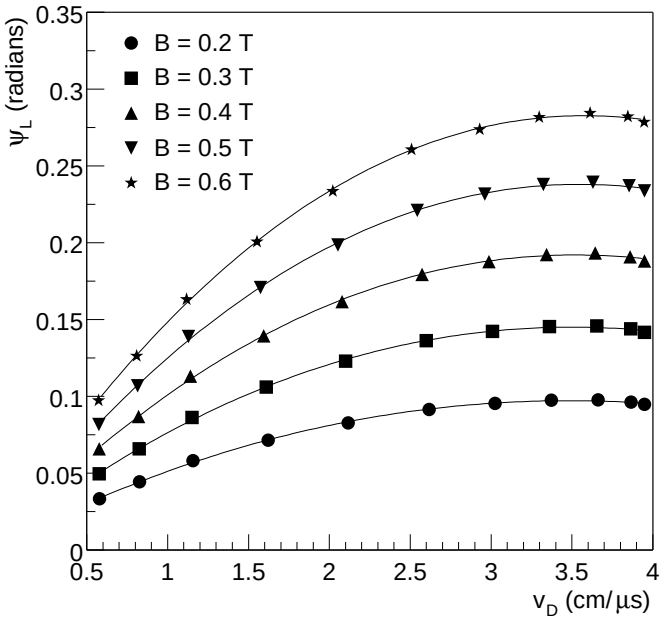

Figure 11.7: The Lorentz angle ψ_{L} as a function of the drift velocity v_{D} for different magnetic field strenghts. The points represent results of a GARFIELD simulation for a Xe,CO_2 (15%) gas mixture. The lines are polynomial fits to the points and are used as parametrization inside AliRoot.

The parameters of the TR photon spectrum for a foil radiator (see Eq. 11.14) have been tuned to approximately reproduce the test beam data at $p = 2\,\mathrm{GeV}/c$ (see Chap. 14), measured with the final much more complicated radiator configuration. Figure 11.6 shows the simulated pion efficiency using the likelihood method on the total charge deposit for different momenta in the ideal case of isolated tracks for the parameters given in Table 11.3. The simulation results are compared with data obtained in prototype tests. Despite reproducing the gross trend of the data, we found it difficult to reproduce the measurements with an unique set of parameters. The parameters were tuned to the data at a momentum of 2 GeV/c , and for the same parameters pion efficiency is sizeably better for the simulations than the data at lower momenta. Also, our simulations show a deterioration of the pion efficiency for higher momenta which is not seen in the data taken from the literature [18].

11.2.3 Signal generation

In the second step the electron clusters (hits in AliRoot) have to be transformed into ADC-like signals (digits). Therefore the charge that the electrons in a given time bin induce on a given pad has to be computed. Apart from summing up the charge deposited by different tracks in one detector pixel (pad and time bin) and transforming it into an ADC channel number, this procedure requires to also take into account all known detector properties.

Diffusion

While drifting through the gas volume the electron cloud, produced at position (x_0, y_0, z_0), is smeared out in space due to diffusion. Its spatial distribution can be described in the following way:

$$P(x,y,z) = \frac{1}{\sqrt{2\pi}\delta_{\mathrm{L}}} \exp\left[-\frac{(x-x_0)^2}{2\delta_{\mathrm{L}}^2}\right] \frac{1}{\sqrt{2\pi}\delta_{\mathrm{T}}} \exp\left[-\frac{(y-y_0)^2}{2\delta_{\mathrm{T}}^2}\right] \frac{1}{\sqrt{2\pi}\delta_{\mathrm{T}}} \exp\left[-\frac{(z-z_0)^2}{2\delta_{\mathrm{T}}^2}\right], \quad (11.17)$$

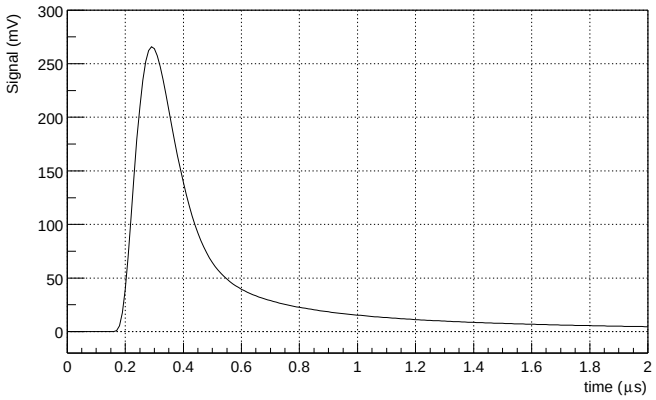

Figure 11.8: The response of the preamplifier shaper (120 ns FWHM, 6.1 mV/fC) to a pad signal simulated with GARFIELD for a 6 keV point charge deposit (corresponding to 9-10 times the signal of a MIP).

with

$$\begin{aligned} \delta_{\mathrm{T}} &= D_{\mathrm{T}}\sqrt{L_{\mathrm{drift}}} \\ \delta_{\mathrm{L}} &= D_{\mathrm{L}}\sqrt{L_{\mathrm{drift}}}. \end{aligned}$$

Here D_{T} and D_{L} denote the diffusion constants in the transverse and longitudinal direction and L_{drift} is the drift length. In order to simulate this effect each electron therefore is assigned a new position according to Eq. 11.17.

E×B effect

For the TRD readout chambers the drift direction is always perpendicular to the magnetic field vector. This means that the drifting electrons will experience a Lorentz force resulting in a displacement of the position in the direction along the wires. For an electron produced at position (x_0, y_0, z_0), where y and z directions are perpendicular to the drift direction along x and the y-axis is parallel to the wires, the new y-position can be calculated by the expression:

$$y = y_0 + \omega\tau\,(x - x_0), \qquad \omega\tau = \tan\psi_{\mathrm{L}}, \tag{11.18}$$

where ψ_{L} is the Lorentz angle. This parameter depends strongly on the strength of the magnetic and electric fields in the readout chamber. Figure 11.7 shows the variation of ψ_{L} with the drift velocity v_{D} for different magentic fields, as calculated by a GARFIELD [20] simulation. These dependencies were parametrized and used inside AliRoot to automatically set the Lorentz angle according to the chosen drift velocity for a given B-field. For the standard combination of $B = 0.4\,\mathrm{T}$ and $v_{\mathrm{D}} = 1.5\,\mathrm{cm}/\mu\mathrm{s}$ this results in a value of $\psi_{\mathrm{L}} = 7.7^{\circ}$ and a maximal displacement of $y_{\max} - y_0 = 0.4\,\mathrm{cm}$ for the full drift length.

Gas gain fluctuations

Each electron arriving at the anode wire creates an avalanche of charge q. The magnitude of the average amplified charge $\bar{q}$ is determined by the applied high voltage. Following [6, 7] the fluctuations of the gas gain are modelled using an exponential distribution:

$$P(q) = \frac{1}{\bar{q}} \exp\left(-\frac{q}{\bar{q}}\right). \tag{11.19}$$

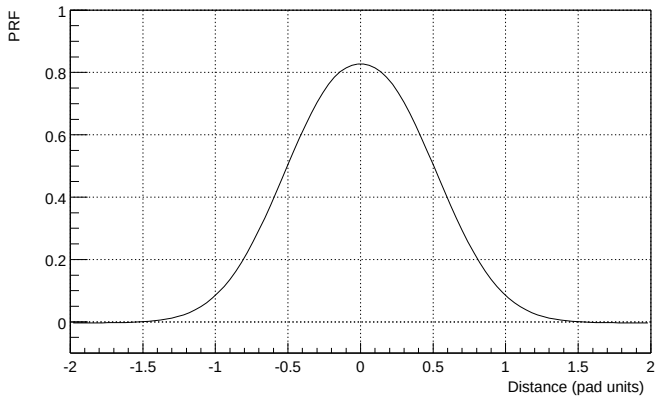

Figure 11.9: The pad response function.

Time response

The signals recorded on the pads are determined by the following effects:

- The slow drift of the Xe ions which introduces a long tail in the time distribution.
- The non-isochronity of the electron drift, depending on the position of the electron relative to the anode wire position.
- The response of the preamplifier shaper to the incoming detector signal.

To determine the total time reponse of the detector and preamplifier to a single electron a simulation has been performed that takes all three effects into account. Figure 11.8 shows the result of a simulation of the preamplifier shaper response to a signal (corresponding roughly to a 6 keV point charge deposit) that has been generated with GARFIELD. This curve, normalized at the maximum to 1, is then used in the digitization part of AliRoot to sample the time distribution of each electron signal according to the given ADC frequency. It is further assumed that due to the shaping the ratio of the integrated charge to the input signal is equal to 0.4.

Pad response

The charge that is induced on the pad plane by the electrons collected at the anode wire is spread over several pads. Using the Mathieson formalism [21], the pad response function (PRF) that describes how the charge is distributed over adjacent pads can be calculated. Figure 11.9 shows the PRF for chevron type pads with a width of $w = 10\,\mathrm{mm}$, a step of $s = 5\,\mathrm{mm}$, and a distance to the wire plane of $h = 2.5\,\mathrm{mm}$, which is used in the current simulations. Note that this PRF is very similar to the one of rectangular pads (see chapters 4 and 14), which are used in the actual pad geometry. A pad coupling factor equal to 0.5 (see section 4.6.3) is applied, which takes into account that only a fraction of the charge collected at the wire is seen by the readout pads.

Electronic noise and conversion gain

To provide a realistic description of the output signal, also the electronic noise has to be included. In the present simulation it is assumed that the noise distribution can be described by a Gaussian with a sigma of $\sigma_{\mathrm{noise}} = 1000\,\mathrm{e}^-$. Following from this the conversion gain of the amplifier is chosen such that σ_{noise} corresponds to ADC channel 1.

Digitization parameters

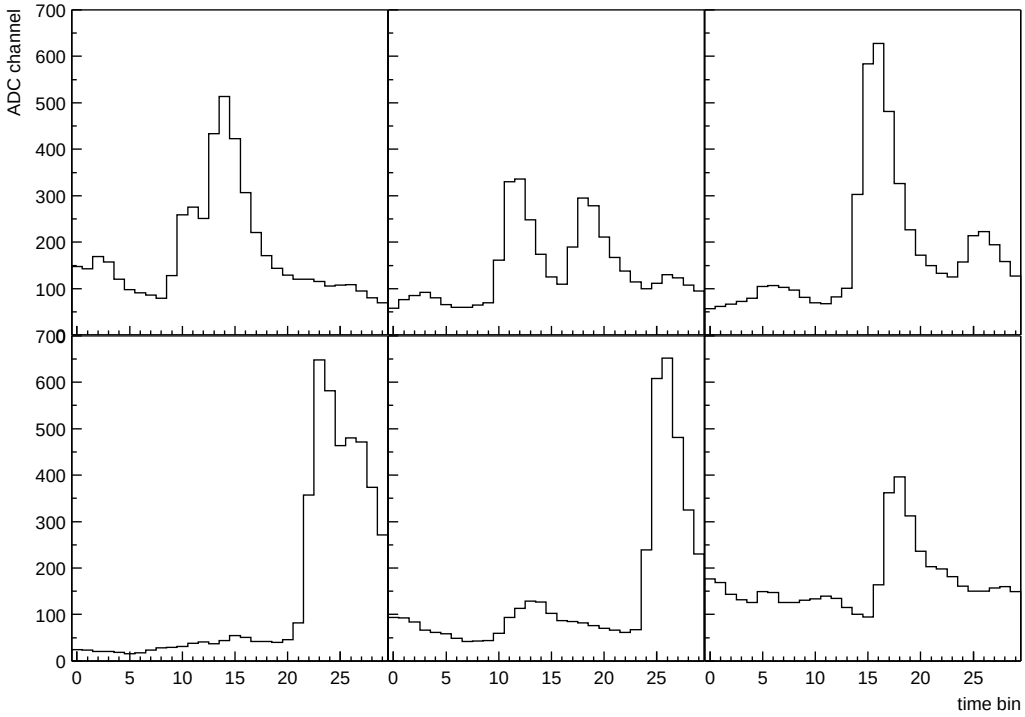

Figure 11.10: A typical sample of signals as a function of the drift time produced by $p = 3.0\,\mathrm{GeV}/c$ electrons in one readout chamber.

Table 11.4: The digitization parameters.

B-field	0.4 T
Drift velocity v_D	1.5 cm /μs
Transverse diffusion coefficient	180 μm /$\sqrt{\mathrm{cm}}$
Longitudinal diffusion coefficient	250 μm /$\sqrt{\mathrm{cm}}$
Lorentz angle ψ_L	7.7°
Gas gain $\bar{q}$	$2.8 \cdot 10^3$
Electronics gain	6.1 mV/fC
Electronics noise σ_noise	1000 e^-
Pad coupling factor	0.5
Time coupling factor	0.4
ADC range	1 V
ADC resolution	10 bit

Table 11.4 summarizes the parameters that are used in the simulation of the TRD response. The diffusion coefficients and the Lorentz angle are determined by the actual values of drift velocity and B-field. The average gas gain is chosen such ($2.8 \cdot 10^3$) that the energy loss signal of a minimum ionizing particle is around ADC channel 40. Figure 11.10 shows some typical electron signals that result from the above described digitization procedure.

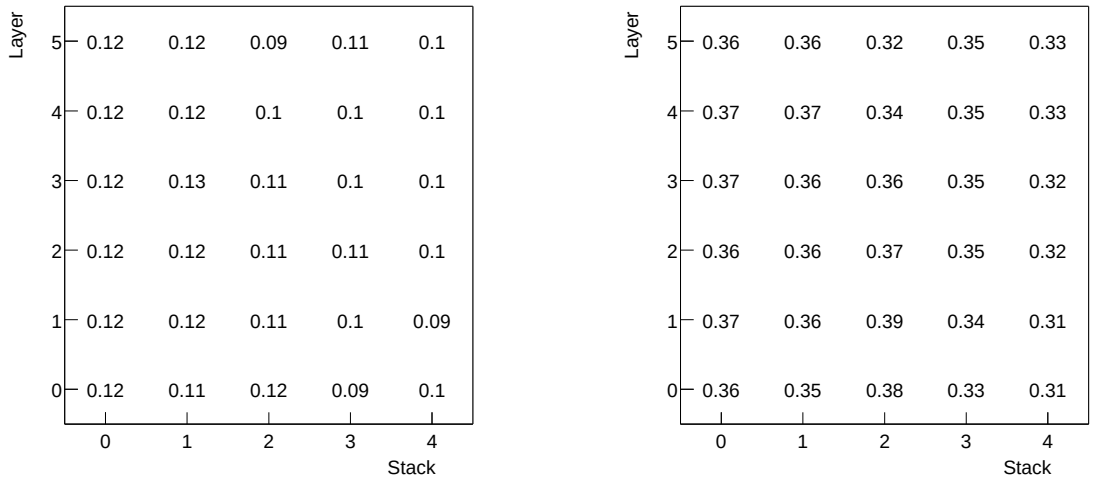

Figure 11.11: The occupancy in different stacks of the TRD for $\mathrm{d}N_{\mathrm{ch}}/\mathrm{d}y = 2000$ (left) and $\mathrm{d}N_{\mathrm{ch}}/\mathrm{d}y = 8000$ (right).

11.3 Point reconstruction

11.3.1 Clustering method

The currently employed clustering mechanism searches for adjacent pads in *y*-direction with a signal above threshold that could form a pad cluster. Since there is only little charge sharing in *z*-direction no clustering is performed here. The same is true for the drift direction, since a track, due to the high ionization in Xe, creates a signal in basically every time bin. Therefore the position of a cluster in *z*- and drift direction is determined by the pad and time bin position. The position in *y*-direction, where a good resolution is mandatory for the momentum measurement, can be extracted with much higher precision, due to the charge sharing. Here one can either calculate the center of gravity of the charge distribution inside a cluster, or use a lookup table to determine the position of the cluster. The latter method, where the position is taken from a table that contains the deviation from the pad center as a function of the ratio of the two largest signals provides generally a better resolution.

Ideally, all clusters contain only signals from two or three pads (2.4 on average for an isolated hit). In the high multiplicity environment of the ALICE experiment, however, there is a large probability that clusters overlap. Currently, only clusters containing signals from five pads are unfolded, using the pad response function as an estimator for the cluster shape. By applying a more sophisticated mechanism one also can disentangle clusters composed of 4 and more pads, thereby reaching a further improvement in resolution at high multiplicity.

11.3.2 Occupancy

The occupancy, defined as the percentage of detector pixels (pad and time bin) with a signal above a threshold (2 ADC-channels), influences crucially the detector performance. Figure 11.11 displays the occupancy numbers in the case of full ($\mathrm{d}N_{\mathrm{ch}}/\mathrm{d}y = 8000$) and quarter ($\mathrm{d}N_{\mathrm{ch}}/\mathrm{d}y = 2000$) multiplicity. The numbers are given for the five stacks in *z*-direction and for the six detector layers. The occupancy is highest for the stack closest to mid-rapidity in the innermost layer. For the middle stack it decreases slightly when going to the outermost layers, while for the more forward stacks no *r*-dependence is visible. In the stack on the side with the absorber for the muon arm (stack 4) a lower occupancy can be observed than in the stack on the other side (stack 0).

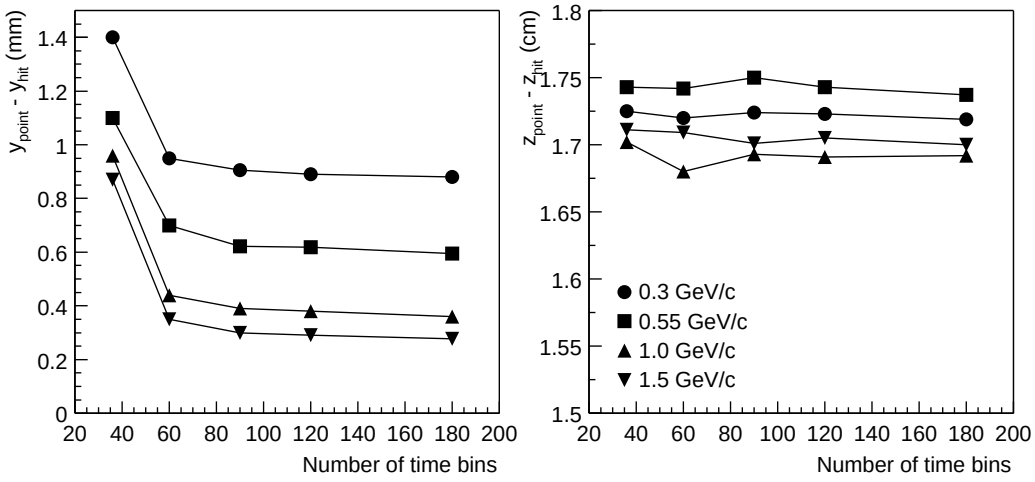

Figure 11.12: The point resolution as a function of the number of time bins for different transverse momenta of the particles (low multiplicity, $dN_{ch}/dy = 150$). The data points are from fits of a Gaussian to the distribution of the difference between simulated and reconstructed position. Only non-overlapping clusters were used.

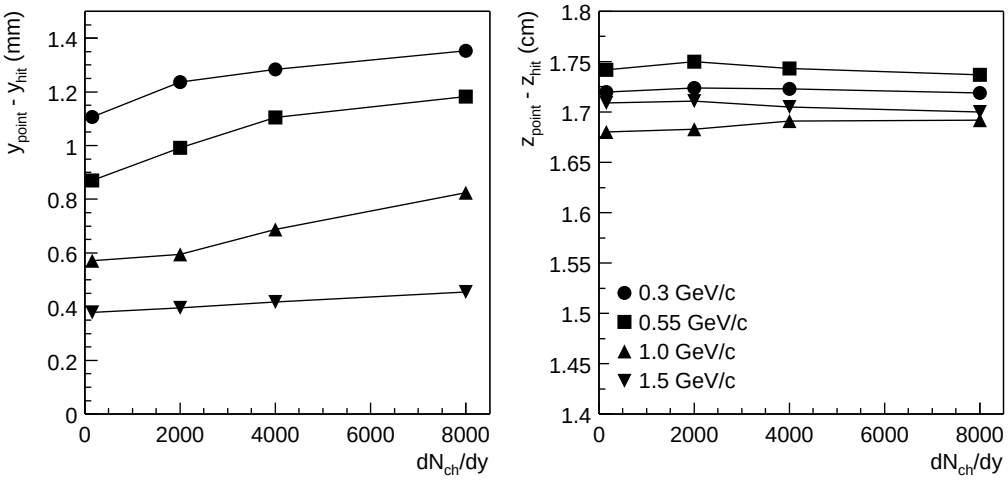

Figure 11.13: The point resolution as a function of the event multiplicity for different transverse momenta of the particles. The data points are from fits using a Gaussian to the distribution of the difference between simulated and reconstructed position. In this analysis also overlapping clusters were included.

11.3.3 Position resolution

Dependence on the number of time bins

One important question is whether there is an optimal choice in the number of time bins. To reduce the data volume, a small number of time bins is preferable. However, any deteriorations in the resolution and efficiencies due to a restricted number of time bins should be minimal. Varying the number of time bins here means to vary the sampling frequency and to keep the drift length constant. Figure 11.12 shows the dependence of the point resolution as a function of the number of time bins in all 6 layers for different transverse momenta. In the left column the difference between the *y*-position of the reconstructed point and the corresponding simulated hit is plotted, while the right column shows the same for the *z*-position. While the *z*-resolution does not depend on the number of time bins, the *y*-resolution is getting worse for less then 60-80 time bins. Based on this result we choose 90 time bins (15 per layer) as default value.

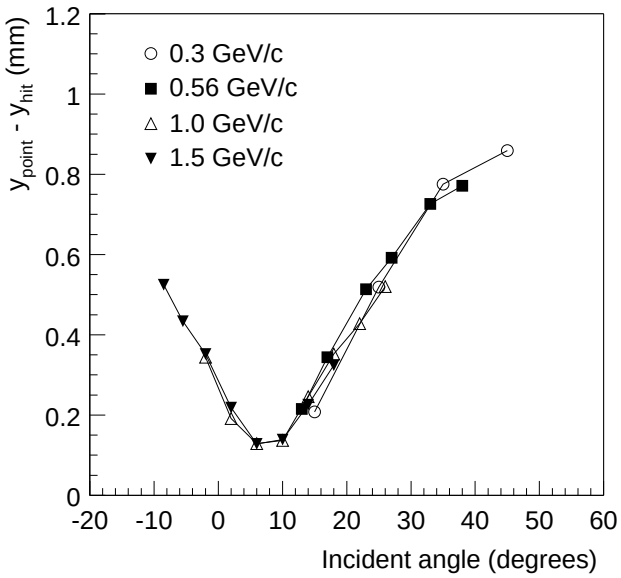

Figure 11.14: The point resolution for positive tracks in *y*-direction as a function of the incident angle for different track total momenta using only non-overlapping clusters (Gaussian fit, low multiplicity, $\mathrm{d}N_{\mathrm{ch}}/\mathrm{d}y = 150$).

The strong momentum dependence is an angular effect as discussed below (see also Fig. 11.14).

Dependence on event multiplicity

Figure 11.13 summarizes how the point resolution depends on the event multiplicity. While a worsening of the resolution in *y*-direction on the order of 10-20% observed, in *z*-direction the resolution is essentially independent of the multiplicity. This is quite understandable since the *z*-resolution is essentially determined by the pad length. In *y*-direction, however, the position is measured via charge sharing between adjacent pads, which is subject to deterioration with increasing occupancy due to overlapping clusters.

Dependence on the track angle

The momentum dependence in the point resolution is mainly caused by the different average incident angles for different momenta. This can be seen from Fig. 11.14, showing that the position resolution in *y* as a function of the incident angle, measured with respect to the normal of the readout chambers, closely follows a unique curve for all tracks, regardless of their momentum. Due to their higher curvature low momentum tracks have a larger incident angle and therefore spread charge over a larger region, resulting in a deteriorated position resolution (see also Fig. 4.16). The optimal resolution is achieved for tracks with an incident angle close to the Lorentz angle $\psi_{\mathrm{L}} = 7.7^{\circ}$, when all the charge produced by the particle is focused on the same point on the anode wire.

11.4 Tracking

11.4.1 Algorithm

Offline tracking in the TRD is based on the Kalman-filtering approach, which we have chosen taking into account the similarities of the tracking environment in the ALICE TPC and in the TRD and based on the successful implementation of the Kalman-filter for tracking in the TPC and ITS. As mentioned in the TPC TDR [5], one of the advantages of the Kalman-filter concept is that it provides a straightforward

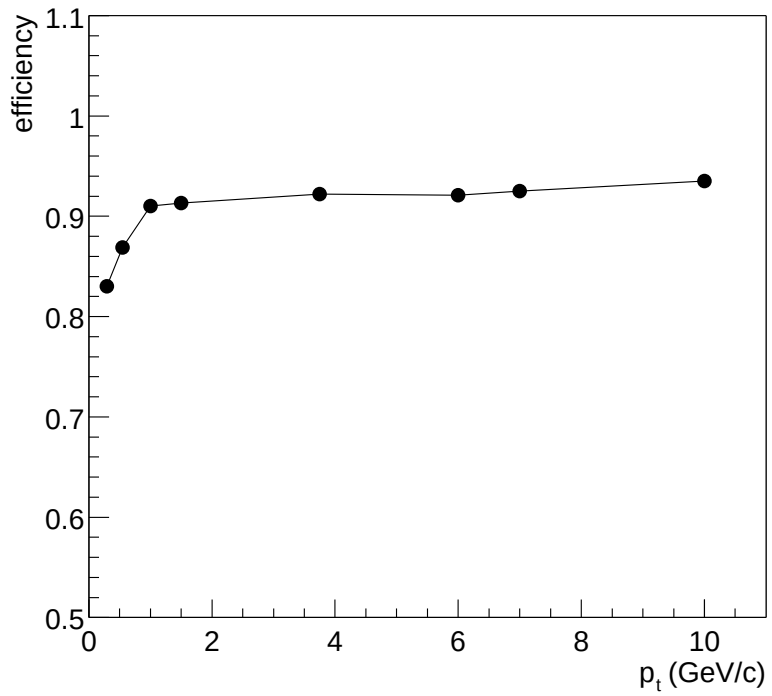

Figure 11.15: The tracking efficiency as a function of the transverse momentum for pion tracks in low multiplicity events ($\mathrm{d}N_{\mathrm{ch}}/\mathrm{d}y = 150$).

way to propagate track segments between subdetectors, in our case between the adjacent TRD layers as well as between the TRD and TPC.

The implementation of the TRD tracking shares many features developed for the ALICE TPC tracking described in detail in the TPC TDR. The tracking starts with finding track seeds in the outermost detector layers. The track candidate is followed inside the drift volume of the readout chambers in steps which correspond to the effective radial distance between two consecutive time bins. At each extrapolation the track helix parameters and covariance matrix are re-evaluated using information about the expected multiple scattering and energy loss. The uncertainties in track parameters define windows along the y and z direction, within which it is checked whether there is a close cluster which can be associated with the track candidate. Since the measurement in z direction is relatively coarse, we first require that the residual in z direction does not exceed half the size of one pad row in z direction. The width of a window in y direction is defined by the uncertainty in the track position and the expected error of the cluster measurement. If two or more clusters are found in a y window, the one closest to the track position is assigned to the track candidate. If no clusters are found in a y window, we repeat the y selection for clusters with residuals in z direction increased to 1.5 times the pad size in z direction. If a close cluster is found, the track parameters and covariance matrix are updated. In the case that no cluster satisfies the above criteria the procedure of track extrapolation and cluster search is allowed to continue for several iterations (due to the dead regions between the sensitive volumes of the readout chambers the allowed gap in the track candidate can be as large as 1.5 times the radial depth of the readout chamber).

11.4.2 Performance

To study the performance of the tracking algorithm, events of different multiplicities up to $\mathrm{d}N_{\mathrm{ch}}/\mathrm{d}y = 8000$ have been simulated with AliRoot using the parametrized HIJING event generator. These events,

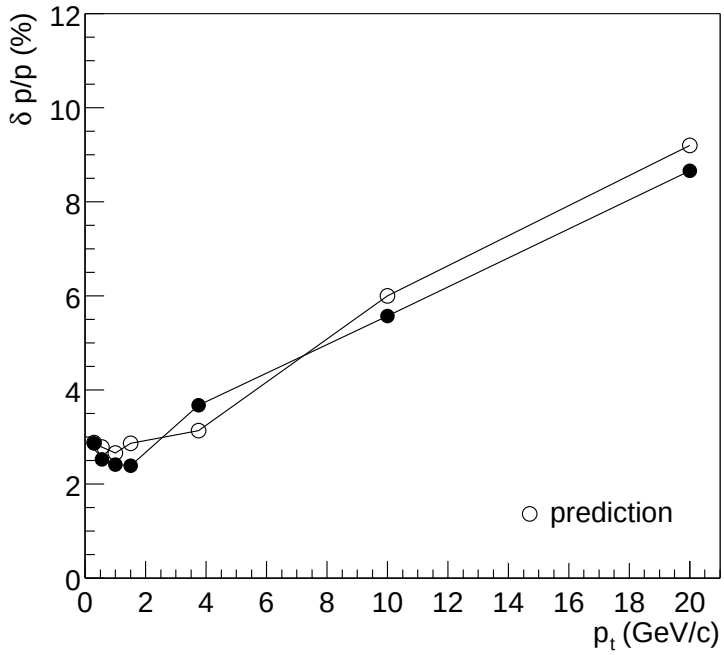

Figure 11.16: The momentum resolution as a function of the transverse momentum for pion tracks in events with low multiplicity ($dN_{ch}/dy = 150$) using a number of time bins of 180. The prediction (open circles) is for the case of 68 independent measurements.

composed of primary pions, kaons, and protons, have been processed through the full reconstruction chain, using the above described procedures.

Efficiency

Figure 11.15 shows the TRD tracking efficiency as a function of the track momentum. This efficiency is defined as the ratio of the number of reconstructed tracks and the number of "trackable" tracks. To fulfill this requirement, a track has to have points in the three outermost layers of the TRD. This definition results in a fraction of $\sim 80\%$ of all charged primary tracks with $45^\circ < \theta < 135^\circ$ and $p_t > 0.2\,\mathrm{GeV}/c$ that are considered as trackable. The analysis shown in Fig. 11.15 was done on events with low multiplicity. For transverse momenta greater than 1 GeV$/c$ the efficiency is above 90%, while it drops sharply when going to lower momenta.

Momentum resolution

The achieved momentum resolution is shown in Fig. 11.16. The extracted points are compared with a prediction for the resolution. This prediction is based on the following formula [22]:

$$(\delta k)^2 = (\delta k_{\mathrm{res}})^2 + (\delta k_{\mathrm{ms}})^2. \tag{11.20}$$

Here δk denotes the error in the track curvature, composed of the contribution from finite measurement resolution δk_{res} and from multiple scattering δk_{ms}. Under the assumption that the total error in the very low momentum regime is dominated by multiple scattering, the latter contribution can be estimated to

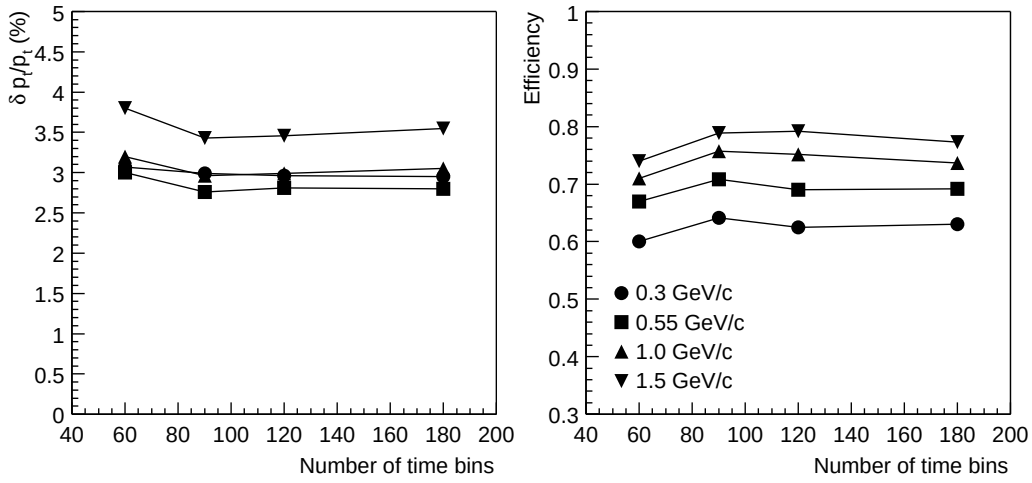

Figure 11.17: The tracking performance for pion tracks as a function of the number of time bins for different tranverse momenta in a high multiplicity environment ($dN_{ch}/dy = 8000$). The left panel shows the resolution in transverse momentum and the right panel the efficiency.

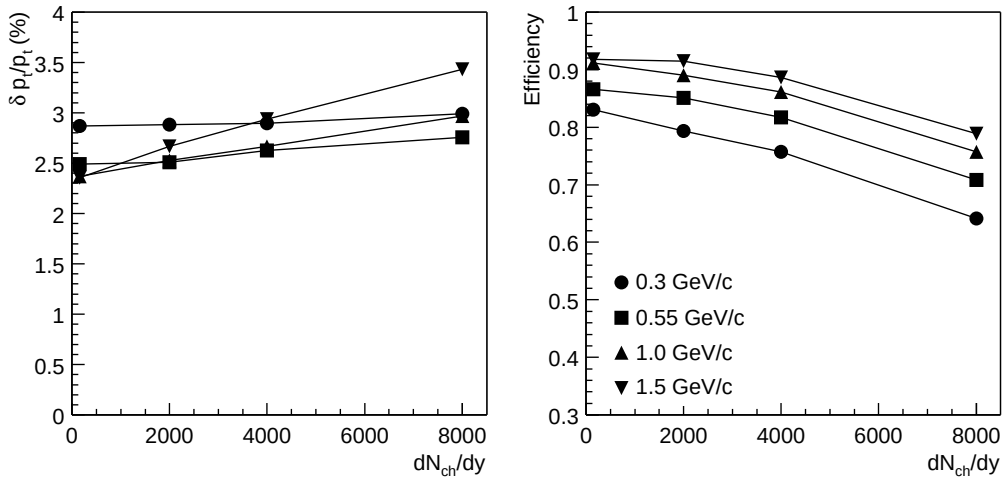

Figure 11.18: The tracking performance for pion tracks as a function of the event multiplicity for different transverse momenta (90 time bins). The left panel shows the resolution in transverse momentum and the right panel the efficiency.

be $\delta k_{\mathrm{ms}} \approx 0.003/p$. The first contribution can be described by:

$$\delta k_{\mathrm{res}} = \frac{\varepsilon}{L'^2}\sqrt{\frac{360}{N+4}}. \tag{11.21}$$

Here N is the number of independently measured points along the track, L' the length of the track projected onto the bending plane, and ε the measurement error for each point, perpendicular to the trajectory. Since L' and ε are known for a given momentum, N can be derived from the momentum dependence of the resolution (the ion tail and the shaping lead to correlations). It is found that a good agreement with the simulations can be achieved by assuming $N = 68$. Since the number of time bins directly determines the maximum number of independently measured points, we conclude, based on this finding and on Fig. 11.12, that a number of time bins of 90 is sufficient to achieve the desired performance of the detector.

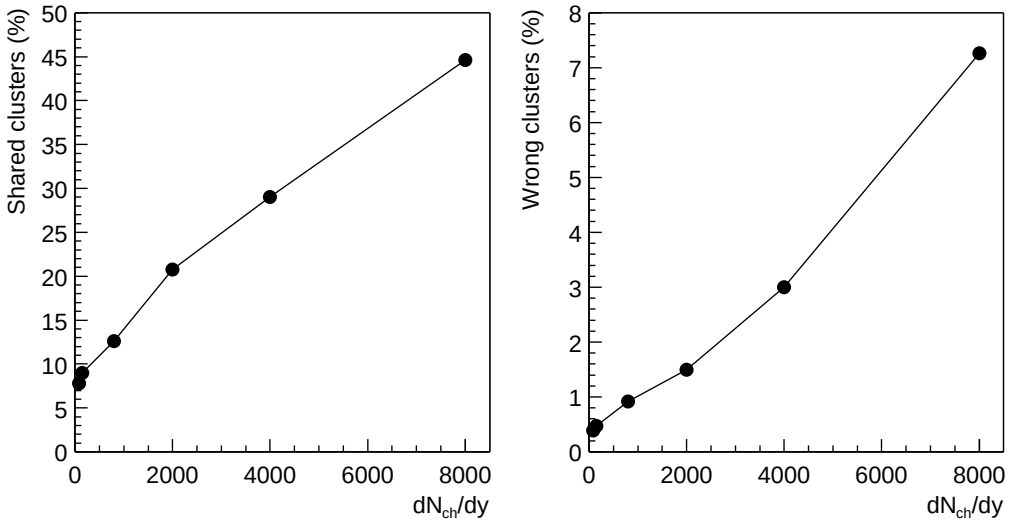

Figure 11.19: The percentage of overlapping clusters (left) and wrongly assigned clusters (right) as a function of the event multiplicity.

Dependence on the number of time bins

The choice of the number of time bins has no significant effect on the offline tracking performance, if the number of time bins is above 80. This is evident from Fig. 11.17, showing the resolution in transverse momentum in the left panel and the tracking efficiency in the right panel as a function of the chosen number of time bins. The same behaviour was already visible in the point resolution of isolated clusters (see Fig. 11.12), which is already constant for more than 60 time bins.

Dependence on event multiplicity

Figure 11.18 summarizes how the tracking performance depends on the event multiplicity. The resolution in transverse momentum deteriorates only slightly, but remains well below 4% at p_{t}= 1.5 GeV$/c$, when going from low multiplicity to the maximum multiplicity of $\mathrm{d}N_{\mathrm{ch}}/\mathrm{d}y = 8000$. The tracking efficiency drops with increasing event multiplicity by $\sim 15\%$ for $p_{\mathrm{t}} = 1.5\,\mathrm{GeV}/c$ and almost $\sim 25\%$ for very low transverse momenta. The reason for this can be seen in Fig. 11.19 that displays in the left panel how the percentage of clusters that have contributions from more than one track increases with the event multiplicity. Similarly, the fraction of points that are assigned to the wrong track increases (right panel). However, a preliminary analysis has shown that by employing a mechanism to unfold overlapping clusters an improvement in the tracking efficiency by $\sim 10\%$ is easily achieved so that efficiencies of about 85% and higher for tracks with $p_{\mathrm{t}} > 1.0\,\mathrm{GeV}/c$ are possible.

11.5 Pion rejection

While test beam results with isolated tracks in the TRD prototypes have shown that a pion rejection factor in the range of 300 to 500 can be achieved (see Chapter 14), the performance of the detector as a function of event multiplicity has to be evaluated using Monte Carlo methods. Therefore the pion rejection factor was studied as a function of the event multiplicity with AliRoot simulations.

In this simulation the parametrized HIJING event generator was used to create a realistic event background, with a full event corresponding to $\mathrm{d}N_{\mathrm{ch}}/\mathrm{d}y = 8000$. Into this background 500 electrons or pions, of a fixed momentum were embedded. These simulated events were then reconstructed with the full reconstruction chain described above. Finally, distributions of the energy deposit were accumulated from

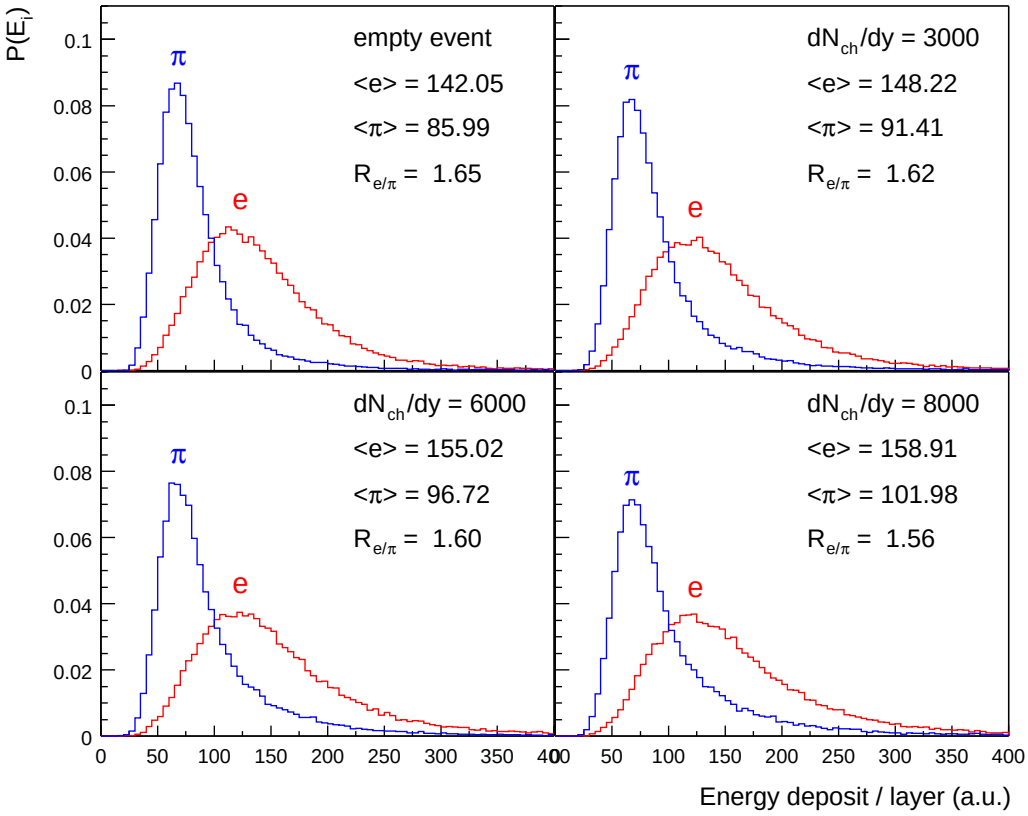

Figure 11.20: The distribution of the deposited energy for electrons and pion of a momentum of $p = 3\,\mathrm{GeV}/c$ after they are reconstructed in events with different multiplicities. The data are corrected for the number of points contributing and for the track inclination.

the clusters assigned to the reconstructed electron (pion) tracks. A track is defined to belong to an electron (pion) if the majority of its points were generated by the input Monte Carlo electron (pion). Using these distributions the pion rejection factor for a specific electron efficiency can be determined by employing the likelihood method (L-Q). A full description of the commonly used methods of extracting the pion rejection factor is given in Chapter 14. This procedure allows to study the degradation of the pion rejection due to the following effects:

- In a high occupancy environment clusters might pick up charge from another particle and therefore the charge measurement gets distorted (see Fig 11.19, left panel). Even when restricting the analysis to small (2 and 3 pad) clusters this effect is visible.

- The tracking algorithm assigns wrong clusters to a given track (see Fig 11.19, right panel), also resulting in an incorrect measurement of the energy deposition.

- Clusters are not found, because their position is distorted, which deteriorates the resolution of the charge measurement.

Figure 11.20 shows the distributions of the reconstructed deposited energy E_i per detector layer i for different event multiplicities. The energy deposit is only calculated using clusters composed of 2 or 3 pads. An additional requirement is that a track has at least 10 points (out of maximal 15) in a given chamber, which removes $\sim 7\%$ of the single measurements for isolated tracks and $\sim 33\%$ in the full

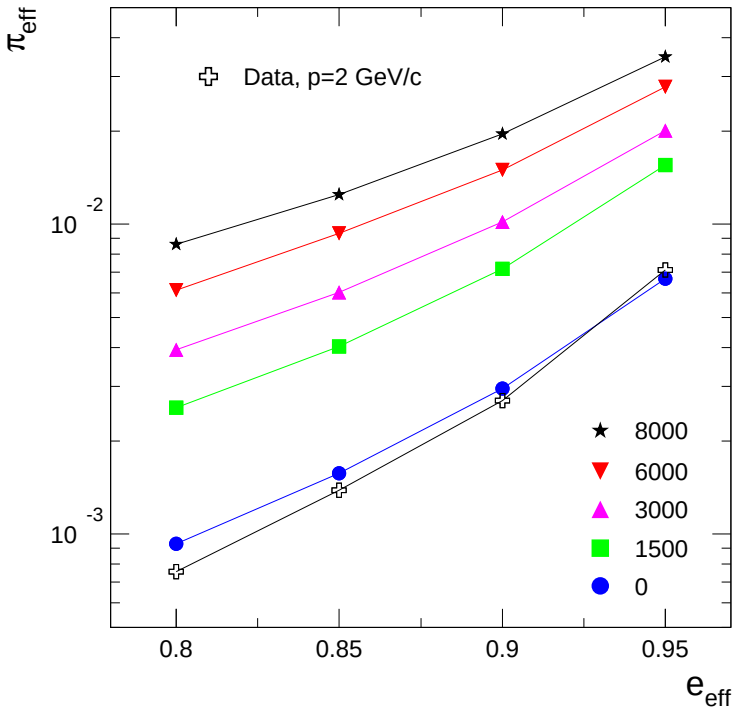

Figure 11.21: The pion efficiency as a function of the electron efficiency for different event multiplicities and tracks of $p = 2\,\mathrm{GeV}/c$ total momentum.

multiplicity case:

$$E_i = 1/N_{\mathrm{points}} \sum_{\mathrm{point}}^{N_{\mathrm{points}}} Q^C_{\mathrm{point}} \qquad \text{with} \qquad N_{\mathrm{points}} > 10. \tag{11.22}$$

Here Q^C_{point} is the corrected charge of a single point. Since a track with non-perpendicular incidence relative to the readout chamber surface deposits more charge in a given time bin than a track that has no inclination, a correction factor, depending on the geometry of the track, has been applied. It can be clearly seen from Fig. 11.20 that the mean energy deposit increases with increasing event multiplicity. This effect is more pronounced for the pions, which, since they have no contribution from TR photon absorption, deposit less energy than the electrons and are therefore stronger affected by threshold effects. The ratio $R_{\mathrm{e}/\pi} = \langle E_{i,\mathrm{e}} \rangle / \langle E_{i,\pi} \rangle$, giving an indication for the rejection power, therefore decreases with increasing event multiplicity.

The effect of this multiplicity dependence of the energy distributions on the pion rejection factor π_{eff} can be seen in Fig. 11.21. The values for π_{eff} have been extracted for different electron efficiencies $\mathrm{e}_{\mathrm{eff}}$ using the distributions shown in Fig. 11.20 as probability distributions. Following the discussion in section 11.2.2 it is evident that the simulation does not reproduce all the available data with a single set of parameters (see Fig. 11.6). Therefore, a calculation of the absolute pion efficiency in the high multiplicity environment from the simulation alone would not be reliable. However, the relative deterioration of the pion efficiency with increasing multiplicity should be described very well. By adjusting the simulation to the test beam data, measured at $p = 2\,\mathrm{GeV}/c$, therefore a good estimate of the achievable pion efficiency at full multiplicity can be derived. Going from well isolated tracks to a full multiplicity event, a worsening of the pion rejection by a factor of 6-7 is observed. For an electron efficiency of 90% the pion efficiency π_{eff} is still about 2% when using the likelihood method on the deposited charge. Therefore even this “worst case” scenario still leads to pion rejection factors close to the desired factor

100 as discussed in chapter 1. As will be shown in chapter 14 a further improvement of 30-40% can be achieved by employing a combined charge/position likelihood analysis.